

# Two-way coupling in active suspensions suppresses particle accumulation and induces non-monotonic flow stabilization

Miyi Wu\*

*High School, California, USA*

Ziyue Yu<sup>†</sup>

*Department of Civil and Environmental Engineering,  
University of Pittsburgh, Pittsburgh, Pennsylvania 15261, USA*

Lei Fang<sup>‡</sup>

*Department of Civil and Environmental Engineering,  
University of Pittsburgh, Pittsburgh, Pennsylvania 15261, USA  
Department of Mechanical Engineering and Materials Science,  
University of Pittsburgh, Pittsburgh, Pennsylvania 15261, USA and  
Department of Bioengineering, University of Pittsburgh,  
Pittsburgh, Pennsylvania 15261, USA*

## Abstract

We experimentally study the two-way coupling between a swarm of centimetre-scale active swimmers (*Artemia salina*) and an electromagnetically driven quasi-two-dimensional cellular flow. The swimmer loading  $N$  and the background forcing  $E$  are varied independently across 85 conditions, and the coupled dynamics are characterized through Lagrangian diagnostics built on the attracting Lagrangian coherent structures (LCS) of the flow. In the dilute limit, swimmers accumulate onto the attracting LCS most strongly when their speed is comparable to the flow speed, recovering the mobility-selective accumulation predicted by one-way-coupled simulations at the fixed aspect ratio of *A. salina*. As the loading increases, this accumulation is progressively suppressed, a collective effect inaccessible to single-swimmer models. The back-action of the swarm on the flow is itself bidirectional and regime-dependent: at low forcing the swarm disorders the attracting-LCS web and scatters the topological critical points of the cellular pattern, whereas at high forcing it reorganizes and reinforces the skeleton. The temporal stability of the skeleton is correspondingly non-monotonic in both  $N$  and  $E$ , with the conditions of maximal stability migrating systematically through the  $(N, E)$  plane. This reinforcement of coherent structures has no counterpart in prior simulations, which reported a predominantly disruptive back-action. Resolving both directions of the coupling shows how collective activity can either erode or reinforce the transport skeleton of a structured flow.

---

\* These authors contributed equally to this work.

† These authors contributed equally to this work.; [ZIY79@pitt.edu](mailto:ZIY79@pitt.edu)

‡ [lei.fang@pitt.edu](mailto:lei.fang@pitt.edu)

## I. INTRODUCTION

Active matter—systems whose constituents convert ambient free energy into self-propelled motion—spans an enormous range of scales, from microscopic bacteria and algae to centimetre-scale crustaceans and metre-scale schooling animals [1–3]. In their natural settings, such swimmers almost never inhabit quiescent fluid: oceans, lakes, and other natural waters are continuously stirred into spatially structured, time-dependent flows, and aquatic organisms must move, feed, and aggregate within them [4]. The mutual interaction between swimming active matter and the flow it inhabits therefore underlies a broad range of transport and mixing processes, yet it remains incompletely understood.

One side of this interaction concerns how a structured background flow organizes the swimmers it carries. Because active particles possess both intrinsic mobility and, typically, an elongated shape, they do not behave as passive tracers: their orientation is set by the competition between self-propulsion and the local strain rate and vorticity, and this coupling produces preferential alignment, mobility-selective clustering, trapping in recirculating regions, and strongly heterogeneous patchiness in turbulence [5–12]. In simple cellular and weakly turbulent flows these effects are especially pronounced, and they have been characterized in detail for the same swimmer–flow system studied here: elongated swimmers preferentially align with, and accumulate along, the attracting material lines of the flow, with the excess concentration collapsing onto a single control parameter combining the swimmer aspect ratio and the mobility ratio  $V_s/U$  [13, 14]; the same alignment governs how swimmers are sorted between regions of differing flow intensity in heterogeneous flow [15]. In all of these studies, however, the flow is treated as a fixed, externally imposed field that acts on the swimmers but is not itself altered by them. Whether this one-way idealization—the flow shapes the swimmers while the swimmers leave the flow untouched—survives in a real, finite-density swarm is far from obvious.

The opposite influence, the back-action of the swimmers on the flow, has been documented largely in isolation. Swimming populations inject energy and momentum into the surrounding fluid, and at the scale of natural waters this biogenic agitation can contribute to turbulence and mixing [16–19]; collective vertical migration can even generate aggregation-scale eddies that restructure a stratified column [20, 21]. At the level of a single swimmer, the biologically generated jet can either intensify or attenuate a background shear depend-

ing on the geometric configuration between the agitation and the shear [22], showing that the back-action reshapes not merely the energy budget of the flow but its spatial organization. In the closest predecessor to the present work, Si and Fang [23] demonstrated that a swarm of brine shrimp can deform the coherent-structure web of an electromagnetically driven cellular flow.

These two directions are not independent: by perturbing the advection, the swimmers act back on the very structures that organize their own distribution, so that the system is intrinsically two-way coupled. This coupling has, however, received little systematic study. The experiment of Si and Fang [23] was confined to a single forcing strength and observed a predominantly disruptive effect, leaving open how the response evolves once both the swimmer loading and the background forcing are varied. Three questions follow directly: whether the one-way accumulation picture still holds in a finite-density swarm; whether the swarm’s effect on the flow is always disordering or can instead be organizing; and what collective behaviour emerges beyond the reach of single-swimmer, one-way models.

Addressing these questions requires making the loosely used notion of a “coherent flow structure” precise. We adopt a Lagrangian description, which intrinsically encodes advection and therefore characterizes transport more faithfully than an instantaneous Eulerian view [24]. Within this framework, Lagrangian coherent structures (LCS)—extracted here as ridges of the finite-time Lyapunov exponent (FTLE) field—are the most strongly attracting and repelling material lines of the flow; they form its skeleton and act as the dominant transport barriers organizing stretching and mixing [24–26]. Because LCS describe the geometry of the flow itself, defined independently of any particle that may populate it, they provide a single language for both directions identified above: the attracting LCS are the lines along which the swimmers accumulate, and they are also the structures whose integrity the swarm may degrade or reinforce. As a complementary, discrete characterization of the same skeleton, we locate the topological critical points of the cellular pattern from its trajectory-curvature field [27]. The quasi-two-dimensional setting we employ is particularly favourable for this purpose, because the inverse energy cascade renders the large-scale coherent structures robust and well defined [28].

In this work we study the two-way coupling experimentally by incorporating a swarm of the centimetre-scale swimmer *Artemia salina* into an electromagnetically driven quasi-two-dimensional cellular flow, spanning a wide range of swimmer loading  $N$  and background

forcing  $E$ . The coupled dynamics are characterized through Lagrangian diagnostics built on the flow skeleton—the FTLE-based attracting LCS and the topological critical points—together with two metrics derived from the attracting LCS: an accumulation coefficient  $CC$  and a stability measure  $R$ . We report two principal findings. First, in the dilute limit we recover the mobility-selective accumulation of the one-way picture, strongest when the swimming speed is comparable to the flow speed and evaluated here at the single fixed aspect ratio of the shrimp; as the loading increases, this accumulation is progressively suppressed—a collective effect inaccessible to single-swimmer, one-way models [13]. Second, the back-action of the swarm on the flow is bidirectional and regime-dependent: depending on the forcing and loading, the swarm either disorders or reinforces the coherent-structure web, with a stability maximum that migrates systematically through the  $(N, E)$  parameter space. The latter behaviour, and in particular the reinforcement of coherent structures, has no counterpart in the predominantly disruptive response reported previously [23].

The remainder of the paper is organized as follows. Section II describes the experimental apparatus and the generation and measurement of the quasi-two-dimensional flow with and without swimmers. Section III introduces the Lagrangian analysis methods, including the FTLE-based detection of attracting LCS, the curvature-based extraction of topological critical points, and the definitions of the accumulation coefficient  $CC$  and the stability measure  $R$ . Section IV presents and discusses the results for both findings, and Section V summarizes our conclusions.

## II. EXPERIMENT METHOD

### A. Apparatus

The background flow is a quasi-two-dimensional (quasi-2D) cellular flow produced by an electromagnetically driven thin-layer system. The apparatus is identical to that used in previous experiments on electromagnetically driven quasi-2D flows and swimmer–flow interactions [15, 23, 29, 30], where it is described in full; here we restate only the parameters needed to reproduce the present experiments. A schematic is shown in Fig. 1a.

A horizontal layer of conducting salt water rests on a tempered-glass floor of  $81.3 \times 81.3 \text{ cm}^2$ , supported by an acrylic body frame of  $96.5 \times 83.8 \text{ cm}^2$ . The upper glass surface is treated with a hydrophobic coating (Rain-X) to reduce friction, and its lower surface is covered with light-absorbing film. Beneath the glass, a checkerboard array of cylindrical permanent magnets (neodymium grade N52; outer diameter 1.27 cm, thickness 0.64 cm, maximum surface flux density 1.5 T per magnet; three magnets stacked per lattice site) is arranged with alternating polarity at a centre-to-centre spacing  $L_m = 5.1 \text{ cm}$ . A pair of copper electrodes on opposite sides of the tank drives a direct current through the fluid layer; the resulting Lorentz force, periodic in sign with the magnet lattice, forces a square array of counter-rotating vortices with cell size  $L_m$ . The vertical field alternates in sign between neighbouring magnets (rendered blue and red in Fig. 1a for field lines pointing into and out of the plane, respectively; the resulting force pattern is indicated for a representative cell), so that the in-plane Lorentz force—and hence the forcing on the fluid—reverses from cell to cell. The working fluid is a 5 mm layer of 14%-by-mass NaCl solution (density  $\rho_f = 1.101 \text{ g cm}^{-3}$ , kinematic viscosity  $\nu = 1.25 \times 10^{-2} \text{ cm}^2 \text{ s}^{-1}$ ). Within this electromagnetically driven layer the flow remains essentially two-dimensional below a critical forcing, a condition satisfied throughout the present experiments [29].

### B. Active matter

The active agents are adult brine shrimp, *Artemia salina*, a centimetre-scale swimmer with a typical body length of about 1 cm. Each animal swims by beating its appendages and generates a propulsive jet directed opposite to its swimming direction, as shown in Fig. 1(c,d). Averaging over five swarming runs at different number densities (no background

flow), the mean single-animal swimming speed is  $V_s = 0.55 \text{ cm s}^{-1}$ , with a run-to-run standard deviation of  $0.08 \text{ cm s}^{-1}$ ; the swimming speed is thus essentially independent of swarm density, justifying its use as a single velocity scale in the mobility ratio  $V_s/U$ .

Because the culturing fluid is less dense than the working fluid, the animals float at the gas–liquid interface and remain in the quasi-2D measurement plane throughout an experiment. Under the spatially uniform illumination used here the animals exhibit no directional bias, so the group is in a *swarming* state: the mean polarization is approximately zero and individual headings are mutually uncorrelated.

### C. Flow characterization and control parameters

The background flow is characterized by its root-mean-square velocity  $U = \sqrt{\langle \mathbf{u} \cdot \mathbf{u} \rangle}$ , where  $\mathbf{u}$  is the measured velocity field and  $\langle \cdot \rangle$  denotes a space–time average. We tune the forcing by varying the dc current from 0.1 to 2.3 A, which raises  $U$  from 0.1 to  $1.75 \text{ cm s}^{-1}$ . With the magnet spacing  $L_m$  as the characteristic length scale, the corresponding Reynolds number  $Re = UL_m/\nu$  ranges from 40 to 700. At the lowest forcing the flow is a steady cellular array; as the current increases the pattern becomes progressively more time dependent. We quantify the strength of the background flow by its mean kinetic energy per unit mass,

$$E = \frac{1}{2} \langle \mathbf{u} \cdot \mathbf{u} \rangle, \quad (1)$$

evaluated from the background flow field. The measurement of  $E$  at each current level is detailed in the experimental protocol (Sec. IID). A natural time unit for the flow is the eddy turnover time  $T_e = L_m/U$ .

The active perturbation is characterized analogously. In the absence of any background forcing, the swarming shrimp drive a flow whose mean kinetic energy per unit mass we denote

$$K_s = \frac{1}{2} \langle \mathbf{u}_s \cdot \mathbf{u}_s \rangle, \quad (2)$$

where  $\mathbf{u}_s$  is the velocity field generated by the shrimp alone (no current). Because  $\mathbf{u}_s$  is measured over the entire swarm,  $K_s$  represents the collective energy injected by all shrimp present and therefore grows with the swimmer number  $N$ ; we find this growth to be linear (Fig. 1e).

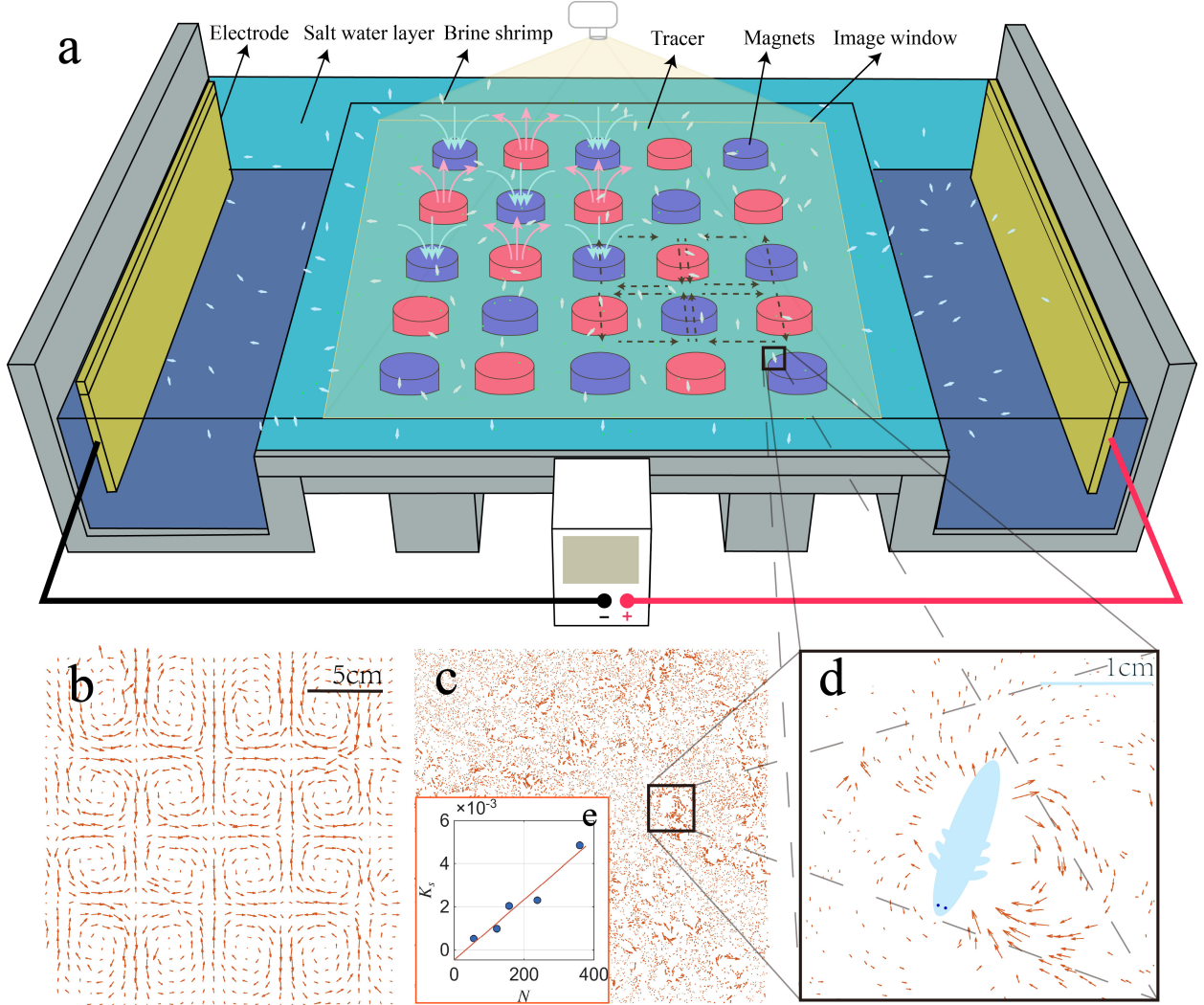


FIG. 1. Experimental setup and representative flow fields. **(a)** Schematic of the electromagnetically driven thin-layer apparatus (not to scale). Blue and red magnets denote field lines pointing into and out of the plane; a representative cell is annotated at the top left, and the black arrows on the lower-right magnet illustrate the flow driven by the resulting Lorentz force. The yellow-shaded region marks the  $21.6 \times 21.6 \text{ cm}^2$  imaging window. **(b)** Background velocity field without shrimp, showing the vortex lattice imposed by the magnets (scale bar 5 cm). **(c)** Instantaneous field with shrimp, combining the cellular flow with swimmer-induced perturbations. **(d)** Zoom-in around a single *A. salina* [boxed region in (c)], showing its recirculating disturbance (scale bar 1 cm). **(e)** Mean kinetic energy  $K_s$  of the shrimp-driven flow (no background current) as a function of swimmer number  $N$ . The solid line is a linear least-squares fit.

The active-flow interaction is governed by two control parameters. The first is the velocity ratio  $V_s/U$ , which compares the single-animal swimming speed  $V_s$  (Sec. II B) with the background flow speed and sets the swimmer mobility relative to the flow. The second is the energy ratio  $K_s/E$ , which compares the active energy injection with the background flow energy. These two are not independent— $K_s/E$  already embeds the speed ratio  $V_s/U$ —and  $K_s/E$  can be varied along two distinct routes: at fixed swimmer number  $N$  by changing the background forcing (and hence  $E$ ), or at fixed  $E$  by changing  $N$  (and hence  $K_s$ ). To disentangle the swimmer loading from the background forcing, we span the parameter space by  $V_s/U$  and the loading-weighted ratio  $NK_s/E$ . It is used here as a convenient coordinate that makes the dependence on swimmer number explicit.

#### D. Experimental protocol

Experiments were conducted in two stages. In the first stage, the background flow was characterized in the absence of shrimp. The working fluid was loaded into the apparatus and the dc current was stepped from 0.1 to 1.6 A in increments of 0.1 A, giving 16 current levels. At each level the flow was allowed to reach a statistically stationary state before 4000 frames were recorded at 60 frames  $s^{-1}$ .

In the second stage, shrimp were introduced into the working fluid and the current sweep was repeated for each of five swimmer-loading levels. The target shrimp numbers were approximately  $N \approx 60, 120, 220, 320,$  and  $410$ , covering nearly an order of magnitude in swimmer loading; the actual number  $N$  in each run was obtained by direct counting of the animals in the recorded images. For each loading level, the animals were allowed to spread uniformly across the imaging domain and reach a swarming steady state before data acquisition began. Each loading level additionally includes a zero-current ( $E = 0$ ) run, in which the swarm drives the flow in the absence of any background forcing; these runs provide the shrimp-only velocity field  $\mathbf{u}_s$  from which the active energy  $K_s$  is calibrated (Sec. II C). For the three lower loading levels ( $N \approx 60, 120,$  and  $220$ ), the dc current was then stepped through the same 0.1–1.6 A sequence and 4000 frames were recorded at each level, giving 17 conditions per loading (the zero-current run plus 16 current levels). For the two higher loading levels ( $N \approx 320$  and  $410$ ), the current range was extended to 0.2–2.3 A in increments of 0.3 A to probe the flow response at stronger background forcing, giving

9 conditions per loading (the zero-current run plus 8 current levels). Shrimp were added cumulatively between loading levels, so that the swimmer number increased monotonically throughout the second stage. In total, the dataset comprises  $16 + 17 \times 3 + 9 \times 2 = 85$  experimental conditions spanning the full  $(N, E)$  parameter space investigated here. The zero-current runs serve only to calibrate the active energy  $K_s$  and are excluded from the parameter-space maps of Figs. 2 and 5, which require a finite background flow ( $E > 0$ ).

### III. ANALYSIS METHOD

All velocity fields were obtained by particle tracking velocimetry (PTV) and interpolated onto a regular Eulerian grid for subsequent analysis (Sec. III A). From these fields we build a set of Lagrangian diagnostics. We first characterize the flow skeleton with two complementary measures: hyperbolic Lagrangian coherent structures (LCSs), identified via the finite-time Lyapunov exponent (FTLE), which mark the most strongly attracting and repelling material lines of the flow (Sec. III B); and the topological critical points of the cellular pattern, extracted from the curvature field of Lagrangian tracer trajectories, which track how the flow topology reorganizes under increasing swimmer loading (Sec. III C). We then quantify the swimmers' effect on this skeleton with two further metrics built on the attracting LCSs: the accumulation coefficient  $CC$ , measuring how strongly the swimmers cluster onto the attracting LCSs (Sec. III D), and the stability  $R$ , measuring how persistent the LCS skeleton is in time (Sec. III E). A natural time unit for all of these is the eddy turnover time  $T_e = L_m/U$ .

#### A. Particle tracking velocimetry and post-processing

The flow was seeded with neutrally buoyant green-fluorescent polyethylene tracers (Spherical; density  $\rho_p = 1.025 \text{ g cm}^{-3}$ , diameter  $d = 106\text{--}125 \text{ }\mu\text{m}$ ). The Stokes number,

$$St = \frac{1}{18} \frac{\rho_p}{\rho_f} \frac{d^2}{L_m^2} Re, \quad (3)$$

is of order  $10^{-4} - 10^{-5}$  across the full range of forcing, confirming that the tracers faithfully follow the fluid motion [31]. The interface was illuminated with blue LED light and imaged from above with a machine-vision camera (Basler acA2040-90  $\mu\text{m}$ ) over a central  $21.6 \times$

21.6 cm<sup>2</sup> region at 1600 × 1600 px, recording on the order of 20000 tracers at 60 frames s<sup>-1</sup> for 4000 frames. Particle positions, velocities, and accelerations were obtained with a particle tracking velocimetry (PTV) algorithm [32].

When shrimp were present in the field of view, the pixels belonging to each *A. salina* were masked to the background intensity before the images were passed to the PTV algorithm, so that only the motion of the fluid tracers—not of the shrimp—was tracked, keeping the recovered velocity field free of swimmer contamination. The scattered velocity vectors were finally interpolated onto a regular Eulerian grid of spacing ≈ 1.25 mm for the field-based diagnostics of Sec. III.

### B. Lagrangian coherent structures and the finite-time Lyapunov exponent

Throughout, we analyse the flow in a Lagrangian frame, which intrinsically encodes advection and therefore gives a more faithful description of transport and mixing than an instantaneous Eulerian view [24]. All Lagrangian fields are built from the flow map

$$\mathbf{F}_{t_0}^t(\mathbf{x}_0) = \mathbf{x}(t; t_0, \mathbf{x}_0), \quad \mathbf{x}(t; t_0, \mathbf{x}_0) = \mathbf{x}_0 + \int_{t_0}^t \mathbf{u}(\tau, \mathbf{x}) d\tau, \quad (4)$$

which we integrate with a second-order Runge–Kutta (Heun) scheme using bilinear interpolation of the measured velocity field in space and time.

Hyperbolic LCSs mark the most strongly attracting, repelling, and shearing material lines of the flow and act as the transport barriers that organize the cellular pattern [24]. We detect them with the finite-time Lyapunov exponent [26]. Following the standard procedure, the flow-map gradient  $\nabla \mathbf{F}_{t_0}^t$  is formed by central differencing of advected tracer pairs with separation 1.25 mm in each direction, and  $\lambda_2$ , the largest eigenvalue of the right Cauchy–Green strain tensor  $\mathbf{C} = (\nabla \mathbf{F}_{t_0}^t)^\top \nabla \mathbf{F}_{t_0}^t$ , gives the FTLE,

$$\text{FTLE}(\mathbf{x}_0) = \frac{1}{|t - t_0|} \frac{1}{2} \ln \lambda_2(\mathbf{x}_0). \quad (5)$$

Ridges of the forward-time field ( $t > t_0$ ) mark repelling LCSs (FTLE<sup>+</sup>); ridges of the backward-time field ( $t < t_0$ ) mark attracting LCSs (FTLE<sup>-</sup>). The flow map is integrated over one eddy turnover time  $T_e$ . The FTLE<sup>-</sup> ridges trace the hyperbolic web that separates the rotational cells; their deformation under increasing swimmer loading is the basis of our flow-response analysis (Fig. 3).

### C. Topological critical points from the Lagrangian curvature field

To track how the topology of the cellular pattern reorganizes—as opposed to how individual ridges deform—we locate the topologically special (stagnation) points of the flow. In the steady, low-Reynolds-number limit the cellular flow is time independent and its topological critical points sit at a regular lattice fixed by the magnet array: a stagnation point at the centre of each vortex and a saddle between neighbouring cells, spaced by  $L_m$ . These lattice points form the most stable topological skeleton the flow can take and serve as a fixed reference against which we assess the instantaneous topology; Within the imaging window we select the thirteen interior lattice points as the fixed reference (the red markers in Fig. 4), excluding those nearest the boundary of the imaging domain whose instantaneous positions can migrate outside the field of view at higher forcing. As the forcing or the swimmer loading increases, the instantaneous critical points unbind from this reference lattice, and we quantify that departure as follows. Following Ouellette and Gollub [27], these points are identified from the curvature of Lagrangian tracer trajectories, which is intense precisely where the trajectory direction turns most sharply, that is, in the vicinity of the critical points of the flow. For a tracer with velocity  $\mathbf{u}$  and acceleration  $\mathbf{a}$ , the trajectory curvature is

$$\kappa = \frac{a_n}{|\mathbf{u}|^2}, \quad a_n = \frac{|u_x a_y - u_y a_x|}{|\mathbf{u}|}, \quad (6)$$

where  $a_n$  is the acceleration component normal to the direction of motion. The pointwise curvature is computed from the PTV velocities and accelerations and gridded onto a mesh of spacing  $\approx 1.25$  mm after removing velocity outliers with an interquartile-range filter.

Topologically special points are then extracted as the high-curvature maxima of a time-smoothed curvature field: the log-curvature  $\log_{10} |\kappa|$  is averaged over a short sliding window of  $\sim T_e/16$  frames and cleaned with an interquartile-range cut; candidate points are taken as connected regions exceeding the 90th percentile of the smoothed field (with small regions and a near-boundary band removed), and each point is located at the curvature-weighted centroid of its region. We do not classify the points further; tracking their number and spatial arrangement as the swimmer loading increases quantifies the reorganization of the flow topology—the unbinding of the critical points from the forced lattice and their pairwise creation and annihilation [27] (Fig. 4). The extracted point pattern is robust to the details of this procedure: varying the smoothing-window length, the percentile threshold, and the grid spacing over the ranges we tested shifts individual point positions only slightly and leaves

the overall count and spatial arrangement—and hence our conclusions about the topological reorganization—unchanged.

#### D. Accumulation near attracting LCSs

To quantify how strongly the swimmers cluster onto the attracting LCSs, we measure the shrimp number density inside the LCS region relative to that over the whole domain. At each instant the attracting-LCS region is defined as the set of grid points whose FTLE<sup>-</sup> value lies in the lowest 15% of the field, i.e. the most strongly attracting ridges (recall that FTLE<sup>-</sup> < 0, so the smallest values mark the strongest attraction); these are the yellow ridges in Fig. 3. A shrimp is counted as belonging to the LCS region when its centroid falls within this region. The accumulation coefficient is then

$$CC = \frac{N_{\text{LCS}}/A_{\text{LCS}}}{N_{\text{tot}}/A_{\text{tot}}}, \quad (7)$$

where  $N_{\text{LCS}}$  is the number of shrimp whose centroids lie within the LCS region of area  $A_{\text{LCS}}$ , and  $N_{\text{tot}}$  and  $A_{\text{tot}}$  are the corresponding totals over the full imaging window. By construction  $CC$  normalizes out the overall swimmer loading:  $CC = 1$  corresponds to a uniform distribution,  $CC > 1$  indicates preferential accumulation on the attracting LCSs, and  $CC < 1$  indicates depletion. We report  $CC$  averaged over all frames of each experimental condition.

#### E. Temporal stability of the flow skeleton

Beyond how the swimmers redistribute within the flow, we ask how stable the flow skeleton itself is in time. We quantify this by the temporal persistence of the attracting-LCS network, which forms the backbone of the cellular pattern. Specifically, we measure the overlap between the LCS regions of two snapshots separated by one eddy turnover time  $T_e$ . Denoting by  $\mathcal{L}(t)$  the attracting-LCS region at time  $t$  (the lowest 15% of the FTLE<sup>-</sup> field, as in Sec. III D), we define the stability  $R$  as their Jaccard index,

$$R = \left\langle \frac{|\mathcal{L}(t) \cap \mathcal{L}(t + T_e)|}{|\mathcal{L}(t) \cup \mathcal{L}(t + T_e)|} \right\rangle_t, \quad (8)$$

where  $|\cdot|$  denotes area and  $\langle \cdot \rangle_t$  is an average over all snapshot pairs in a run. By construction  $0 \leq R \leq 1$ :  $R \rightarrow 1$  indicates a skeleton that barely moves over an eddy turnover time (a

stable, persistent pattern), whereas  $R \rightarrow 0$  indicates one that reorganizes completely (an unstable pattern). The construction is illustrated in Figs. 5(b–d): panel (b) shows the attracting-LCS region  $\mathcal{L}(t)$  at time  $t$ , panel (c) shows  $\mathcal{L}(t + T_e)$  one eddy turnover later, and panel (d) overlays the two masks, with the intersection  $\mathcal{L}(t) \cap \mathcal{L}(t + T_e)$  in grey, the region exclusive to  $\mathcal{L}(t)$  in blue, and the region exclusive to  $\mathcal{L}(t + T_e)$  in red; the example shown has  $R = 0.12$ , indicating a substantially reorganized skeleton.

We use the overlap of the thresholded LCS *masks* rather than a direct correlation of the full FTLE<sup>-</sup> fields, because the latter conflates skeleton stability with the small-scale fluctuations injected by the swimmers. A dense swarm sprinkles the field with short-lived, small-amplitude ridges; these lower the field-to-field correlation even when the underlying backbone is in fact more persistent. The 15% mask isolates the dominant skeleton from this fine-scale noise, so that  $R$  reflects the stability of the flow structure rather than the activity of the swimmers. As an illustration, a direct correlation would rank the shrimp-free case Fig. 3(c) as more stable than the dense-swarm case Fig. 3(i), whereas the skeleton in (i) is in fact the more persistent of the two—a distinction the mask-based  $R$  captures correctly. Both  $CC$  and  $R$  are defined through the same 15% FTLE<sup>-</sup> threshold that isolates the dominant attracting skeleton. We verified that neither diagnostic depends sensitively on this particular value: varying the threshold over a reasonable range rescales the absolute magnitudes of  $CC$  and  $R$  but preserves their dependence on  $N$  and  $E$ , so that all trends reported below are unaffected. The topological critical points of Fig. 4 provide an independent, complementary confirmation of this skeleton stability.

## IV. RESULT AND DISCUSSION

Having established our diagnostics in Sec. III, we now use them to characterize the two-way coupling between the swarming shrimp and the background flow, addressing two complementary questions. The first (Sec. IV A) concerns how the swimmers respond to the flow: how strongly they accumulate onto the attracting LCSs, and how this accumulation changes with swimmer loading, quantified by the accumulation coefficient  $CC$  (Fig. 2). The second (Sec. IV B) concerns how the swimmers in turn reshape the flow skeleton: we first follow the qualitative response of the attracting-LCS ridges (Fig. 3) and of the topological critical points of the cellular pattern (Fig. 4), and then quantify how the temporal persistence of the skeleton varies across the  $(N, E)$  parameter space through the stability metric  $R$  (Fig. 5). Together the two questions trace the bidirectional coupling between an active suspension and a structured background flow.

### A. Density-dependent suppression of accumulation

A prior numerical study established that non-spherical swimmers in a structured flow do not distribute uniformly but instead align with, and accumulate onto, the attracting LCSs of the flow [13]. That study used a hybrid approach: virtual rod-like swimmers were advected through an experimentally measured velocity field and reoriented by the local velocity gradients through Jeffery’s equation, under the assumption of one-way coupling, in which the swimmers are passively transported and reoriented by the flow but do not themselves modify it. Within this one-way picture, the strength of the resulting accumulation was found to depend on the swimmer mobility, being most pronounced when the swimming speed is comparable to the flow speed.

Our experiments reproduce this behaviour and confirm that it holds in a real swarm, as long as the swimmers remain dilute. Figure 2(a) maps the accumulation coefficient  $CC$  (Eq. 7) across the  $(NK_s/E, V_s/U)$  plane. At low loading [the low- $NK_s/E$  region, red box in Fig. 2(a)] the shrimp clearly accumulate on the attracting LCSs, with  $CC > 1$  rather than the uniform value  $CC = 1$ . The dependence on mobility likewise matches the one-way prediction: within this dilute bin,  $CC$  rises to a maximum at intermediate  $V_s/U$  and falls off on either side [Fig. 2(c)], so that the strongest clustering occurs when the swimming

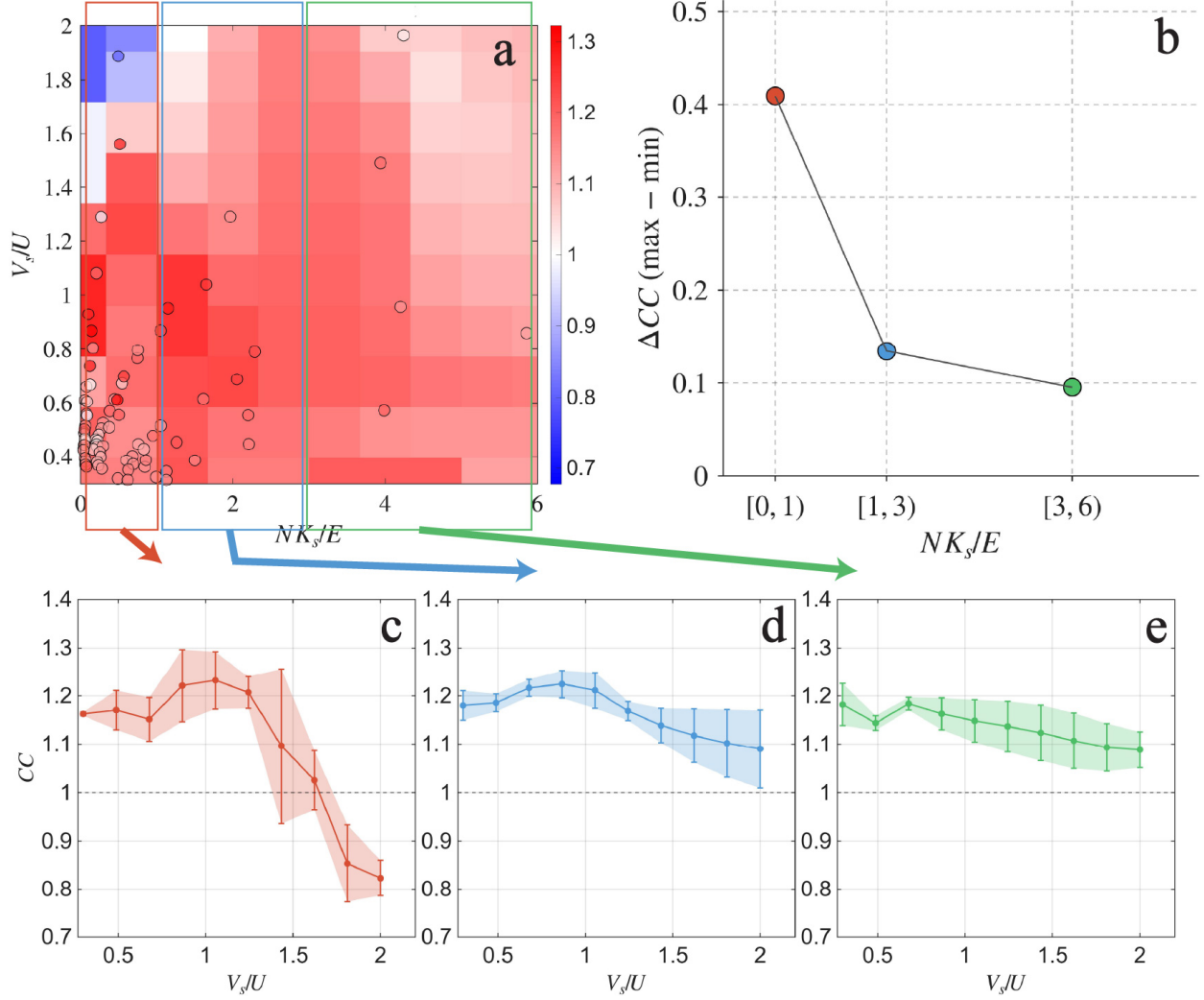


FIG. 2. Accumulation effect as a function of the control parameters  $NK_s/E$  and  $V_s/U$ . **(a)** Heat map of the accumulation coefficient  $CC$  (Eq. 7) in the  $(NK_s/E, V_s/U)$  plane. Triangles mark the measured experimental conditions, coloured by their measured  $CC$ ; the surrounding field is obtained by interpolation. Warmer colours denote stronger accumulation onto the attracting LCSs ( $CC > 1$ ), cooler colours denote depletion ( $CC < 1$ ). The red, blue, and green boxes outline the three  $NK_s/E$  ranges examined in (c–e). **(b)** Accumulation range  $\Delta CC = CC_{\max} - CC_{\min}$ , taken over  $V_s/U$  within each  $NK_s/E$  bin, versus  $NK_s/E$ . **(c–e)**  $CC$  versus  $V_s/U$  for the three bins outlined in (a): **(c)**  $NK_s/E \in [0, 1]$ , **(d)**  $NK_s/E \in [1, 3]$ , and **(e)**  $NK_s/E \in [3, 6]$ . Markers and error bars give the mean and standard deviation within each bin, shaded bands indicate the spread, and the dashed line marks  $CC = 1$ .

speed is comparable to the background flow speed. A competition between mobility and flow straining underlies this optimum—swimmers that are too slow are carried passively and rarely reach the attracting ridges, while swimmers that are too fast pass through the straining regions before the flow can capture them—leaving an intermediate mobility at which retention on the attracting LCSs is most effective.

This dilute picture, however, does not survive once the swarm is dense enough that the swimmers appreciably perturb the background flow themselves. As the loading increases, the agents inject a growing amount of energy into the flow, and the accumulation is progressively lost. This is visible directly in the heat map of Fig. 2(a), where  $CC$  weakens from left to right, and in the flattening of the  $CC-V_s/U$  curves across the three loading bins [Fig. 2(c–e)]: the pronounced mobility-selective peak of the most dilute bin (c) is progressively washed out, until at the highest loading (e)  $CC$  is nearly independent of  $V_s/U$  and only weakly above unity. The accumulation range  $\Delta CC = CC_{\max} - CC_{\min}$ , taken over  $V_s/U$  within each bin [Fig. 2(b)], quantifies this trend:  $\Delta CC$  decreases monotonically with  $NK_s/E$ , from  $\approx 0.4$  in the most dilute bin to  $\approx 0.1$  at the highest loading. The mobility-selective accumulation that governs the dilute limit is thus progressively suppressed as the swimmer loading grows. This density-dependent suppression is a collective effect that lies beyond the reach of single-swimmer, one-way models, and it coincides with the regime in which the swimmers begin to reshape the flow skeleton itself, as we show next.

## B. Regime-dependent stabilization of the flow skeleton

We now turn the question around and ask how the swarm acts back on the flow. The swimmers clearly deform the attracting-LCS skeleton, but the deformation is not always destructive: depending on the background forcing, the swarm can either disorder or reinforce the coherent-structure web.

The full picture emerges on comparing the three swimmer-loading levels across Figs. 3 and 4, where  $E$  increases from left to right within each level. For the shrimp-free flow [(a)–(c)] the skeleton simply degrades with increasing  $E$ , the cellular web breaking up and the critical points spreading as the flow becomes time dependent. Adding swimmers changes this systematically: at low  $E$ , the swarm amplifies the disorder already present in the shrimp-free skeleton, tangling the LCS web further and scattering the critical points [(a)→(d)→(g)]; at intermediate  $E$ , a moderate swarm sharpens the skeleton relative to the shrimp-free case while a dense swarm degrades it again, producing a non-monotonic response [(b)→(e)→(h)]; and at high  $E$ , where the shrimp-free flow is itself disorganized, the swarm restores order, leaving cleaner ridges and more tightly clustered critical points than the corresponding shrimp-free baseline [(c)→(f)→(i)]. A direct comparison at nearly matched forcing underscores the reversal: at  $E = 0.82$  [Fig. 3(c)] the shrimp-free skeleton is already disordered, yet at  $E = 0.77$  [Fig. 3(i)]—a difference of less than 7%—the dense swarm leaves a markedly *more* organized pattern. The disruption-versus-reinforcement balance therefore depends jointly on the forcing and the loading; we quantify it through the temporal stability metric  $R$  below.

Figure 5(a) maps  $R$  across the  $(E, N)$  plane, with the triangles marking the nine representative conditions of Figs. 3 and 4. Reading the map at fixed swimmer number reveals a non-monotonic, loading-dependent response. In the shrimp-free flow ( $N = 0$ )  $R$  decreases monotonically with  $E$ , as the background pattern evolves from a steady cellular array through a transitional regime toward weak turbulence and its skeleton becomes progressively less persistent. At moderate loading ( $N \approx 50$ –150), however,  $R$  first rises and then falls as  $E$  increases, so that the skeleton is most persistent at an intermediate forcing rather than at the lowest one; the swimmers stabilize the skeleton over a band of  $E$ , and the forcing at which stability peaks is shifted to higher  $E$  relative to the dilute case. At still higher loading this peak continues to migrate toward higher  $E$ , while the overall stability

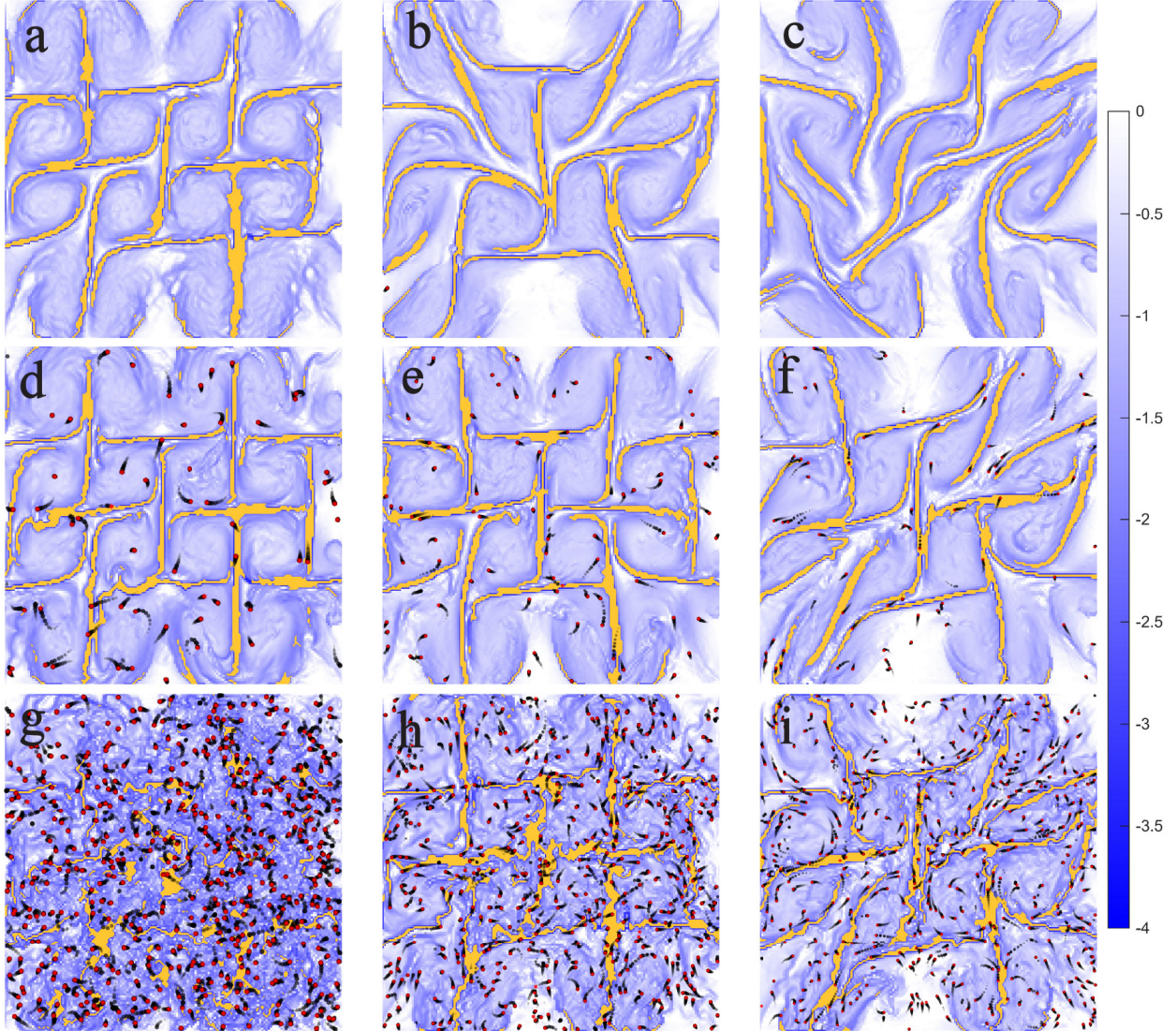


FIG. 3. Attracting LCSs under increasing background forcing  $E$  and swimmer loading  $N$ . In each panel the blue colour shows the  $\text{FTLE}^-$  value (colour bar), and the yellow region marks its lowest 15%, i.e. the most strongly attracting ridges (cf. Sec. III D). Columns correspond to increasing  $E$  from left to right; rows correspond to increasing  $N$  from top to bottom. (a–c) Shrimp-free background flow ( $N = 0$ ) at  $E = 0.06, 0.30,$  and  $0.82$ . (d–f) Low swimmer loading ( $N \approx 60$ ) at  $E = 0.04, 0.24,$  and  $0.79$ . (g–i) High swimmer loading ( $N \approx 410$ ) at  $E = 0.02, 0.26,$  and  $0.77$ . Red dots mark the shrimp centroids and the short black trails their recent trajectories.

decreases, as the increasingly energetic swarm disorders the skeleton across the whole range. Reading the map at fixed forcing tells the same story from the orthogonal direction: the dependence of  $R$  on  $N$  is non-monotonic over an intermediate band of  $E$  and the loading at

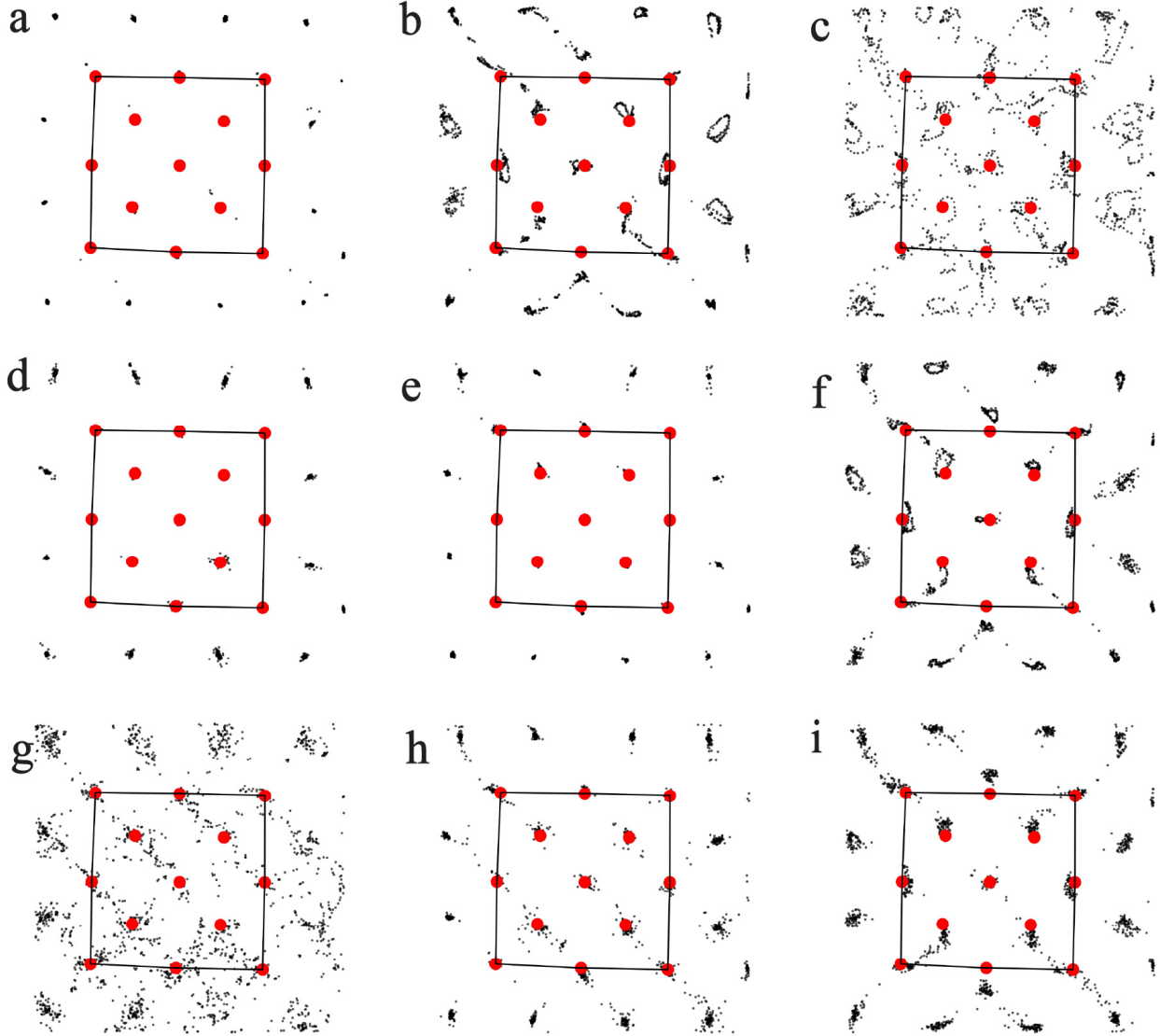


FIG. 4. Topological critical points of the flow under the same  $(N, E)$  conditions as Fig. 3. Red dots mark the thirteen fixed points of the steady, low-Reynolds-number cellular flow imposed by the  $L_m = 5.1$  cm magnet lattice. The solid square simply encloses these reference points. Black dots are the instantaneous critical points extracted frame by frame (Eq. 6, Sec. III C) over 4000 frames and overlaid at fixed intervals. Tightly clustered black points sitting close to the red fixed points indicate a stable topological skeleton, whereas scattered black points lying far from the red references indicate a disordered, unstable skeleton.

which stability is greatest likewise migrates as  $E$  is varied.

We emphasize that two distinct effects contribute to the variation of  $R$  with  $E$ : the

swimmers' action on the skeleton, and the intrinsic time dependence of the background flow, which by itself lowers  $R$  as the forcing increases (the monotonic  $N = 0$  baseline). The signature of swimmer-induced stabilization is therefore not the absolute value of  $R$  but its departure from this baseline—at moderate and high  $E$  the swarm raises  $R$  above the corresponding shrimp-free value. This enhancement is modest in magnitude: even though  $R$  is built from the overlap of thresholded LCS masks rather than a direct correlation of the FTLE<sup>-</sup> fields, the small-scale perturbations continuously injected by the swarm still leave a residual imprint on the metric, partially offsetting the stabilization of the underlying skeleton. The effect is nonetheless systematic and is corroborated by the topological critical points of Fig. 4, which condense toward the reference lattice in precisely the same regimes.

The binned curves of Fig. 5(e–n) confirm these trends statistically. The  $R$ – $N$  curves within fixed  $E$  bands [Fig. 5(e–i)] are monotonically decreasing at the lowest  $E$  but develop an interior maximum at intermediate  $E$ , and the  $R$ – $E$  curves within fixed  $N$  bands [Fig. 5(j–n)] sharpen from a monotonic decay at  $N = 0$  into a peaked form at finite loading, with the peak located at progressively higher  $E$  as  $N$  increases. The non-monotonic, regime-dependent stabilization and the systematic migration of the stability maximum are thus borne out by both the spatial maps and the binned statistics.

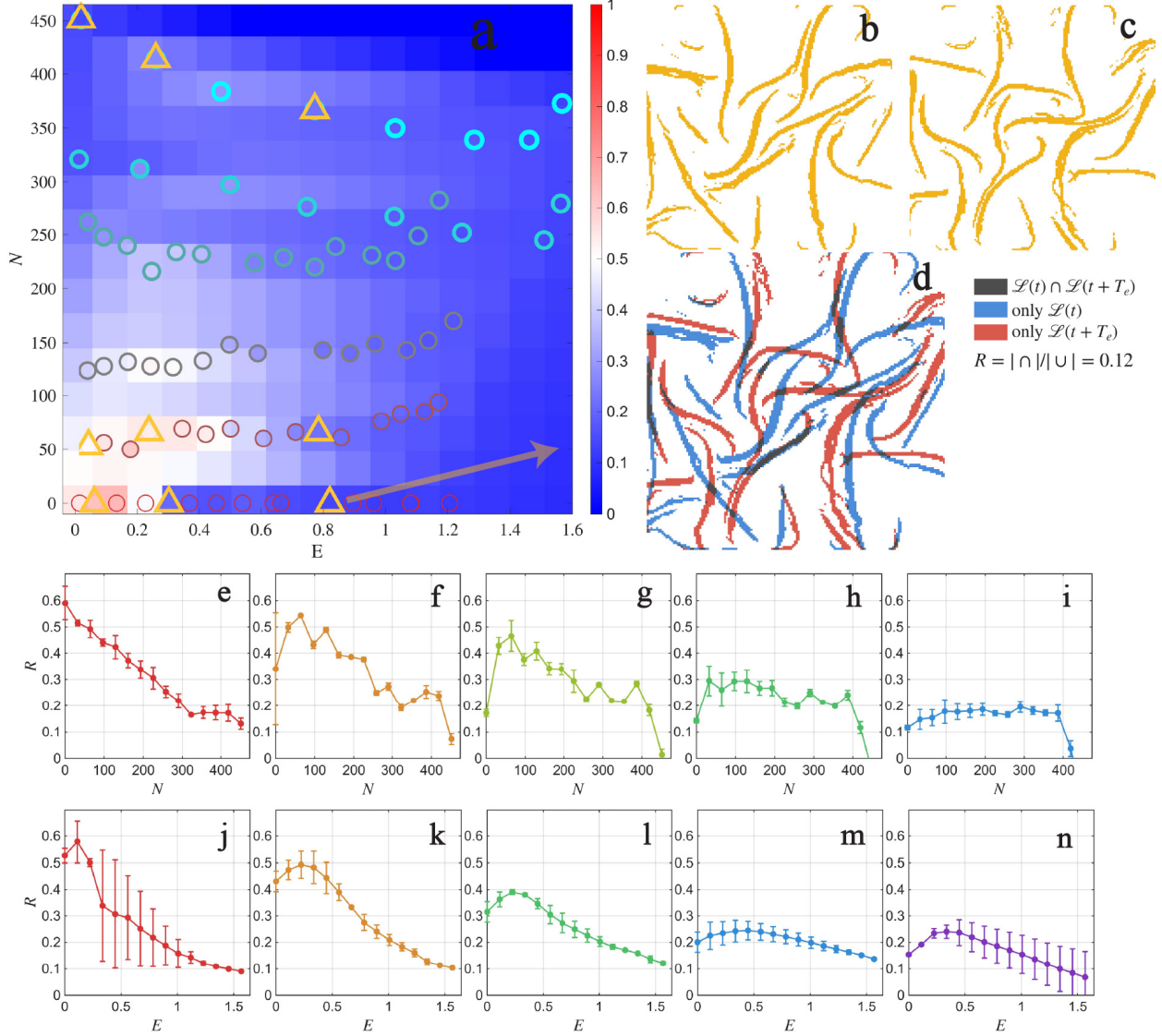


FIG. 5. Temporal stability  $R$  of the flow skeleton (Eq. 8) across the  $(E, N)$  parameter space, where  $E$  is the background forcing and  $N$  the swimmer number. (a) Heat map of  $R$ ; the background colour shows  $R$  (colour bar), obtained by interpolation. Circles mark all measured conditions and triangles the nine representative cases of Figs. 3 and 4; the symbols are coloured separately, by swimmer number  $N$ , from red ( $N = 0$ ) to cyan (highest  $N$ ). (b–d) Illustration of the stability metric for a single condition. (b) The attracting-LCS region  $\mathcal{L}(t)$  at one instant and (c) the region  $\mathcal{L}(t + T_e)$  one eddy turnover time later (yellow, the lowest 15% of the FTLE<sup>-</sup> field). (d) Their overlap: the intersection  $\mathcal{L}(t) \cap \mathcal{L}(t + T_e)$  (grey), the part only in  $\mathcal{L}(t)$  (blue), and the part only in  $\mathcal{L}(t + T_e)$  (red). (e–i)  $R$  versus  $N$  within fixed  $E$  bins:  $E \in [0, 0.2]$ ,  $[0.2, 0.4]$ ,  $[0.4, 0.6]$ ,  $[0.6, 1.0]$ , and  $[1.0, 1.4]$ . (j–n)  $R$  versus  $E$  within fixed  $N$  bins:  $N \in [0, 35]$ ,  $[35, 150]$ ,  $[150, 250]$ ,  $[250, 350]$ , and  $[350, 450]$ . Markers and error bars give the mean and standard deviation within each bin.

## V. CONCLUSION AND SUMMARY

We have experimentally investigated the two-way coupling between a swarm of centimetre-scale swimmers and a structured background flow. Brine shrimp (*A. salina*) were introduced into an electromagnetically driven quasi-2D cellular flow, and the swimmer loading and the background forcing were varied independently across the full  $(N, E)$  parameter space. Using a set of Lagrangian diagnostics built on the attracting LCSs and on the topological critical points of the flow, we characterized both how the swimmers organize within the flow and how they reshape the flow in return.

We first quantified the accumulation of swimmers onto the attracting LCSs. In the dilute limit our measurements reproduce the mobility-selective accumulation predicted for non-interacting swimmers [13]: clustering onto the attracting LCSs is strongest when the swimming speed is comparable to the flow speed. As the swarm becomes denser, however, this accumulation is progressively suppressed—the mobility-selective signal flattens and the distribution returns toward uniformity. This density-dependent weakening is a collective effect that lies outside the reach of single-swimmer models.

We then examined how the swarm acts back on the flow skeleton. Its influence is bidirectional and regime-dependent: at low forcing the swarm disorders the attracting-LCS web and scatters the topological critical points, whereas at high forcing—where the unforced flow is itself disorganized—the swarm reorganizes the skeleton, sharpening the ridges and drawing the critical points back toward the forced lattice. The temporal stability of the skeleton is correspondingly non-monotonic in both loading and forcing, and the conditions of maximal stability migrate systematically through the  $(N, E)$  plane. The field-based and topological diagnostics agree on this picture.

Taken together, the two results trace the bidirectional coupling between an active suspension and a structured flow: the swimmers respond to the flow by accumulating onto its coherent structures, and the flow responds to the swimmers as its skeleton is alternately disrupted and reinforced. Earlier one-way-coupled descriptions capture only the first of these, and only in the dilute limit; resolving both directions, together with their dependence on loading and forcing, is essential to understanding how active agents reshape the transport structure of the flows they inhabit. The regime-dependent stabilization in particular suggests that active matter might be used either to break down or to reinforce transport

barriers, depending on the balance between activity and background forcing.

Several questions remain open. A full mechanistic account of the regime-dependent skeleton response—in particular why activity disorders the skeleton at low forcing but reinforces it at high forcing—remains to be established and is the subject of ongoing work. Our diagnostics characterize the geometry and persistence of the flow skeleton rather than transport itself; relating the observed reshaping of the skeleton to direct measurements of mixing and dispersion is a natural next step. Finally, extending the present study to stronger, fully turbulent background flows would test how robust the regime-dependent coupling is beyond the weakly time-dependent regime probed here.

- 
- [1] S. Ramaswamy, The mechanics and statistics of active matter, [Annu. Rev. Condens. Matter Phys. \*\*1\*\*, 323 \(2010\)](#).
- [2] M. C. Marchetti, J. F. Joanny, S. Ramaswamy, T. B. Liverpool, J. Prost, M. Rao, and R. A. Simha, Hydrodynamics of soft active matter, [Rev. Mod. Phys. \*\*85\*\*, 1143 \(2013\)](#).
- [3] C. Bechinger, R. Di Leonardo, H. Löwen, C. Reichhardt, G. Volpe, and G. Volpe, Active particles in complex and crowded environments, [Rev. Mod. Phys. \*\*88\*\*, 045006 \(2016\)](#).
- [4] J. S. Guasto, R. Rusconi, and R. Stocker, Fluid mechanics of planktonic microorganisms, [Annu. Rev. Fluid Mech. \*\*44\*\*, 373 \(2012\)](#).
- [5] C. Torney and Z. Neufeld, Transport and aggregation of self-propelled particles in fluid flows, [Phys. Rev. Lett. \*\*99\*\*, 078101 \(2007\)](#).
- [6] N. Khurana, J. Blawdziewicz, and N. T. Ouellette, Reduced transport of swimming particles in chaotic flow due to hydrodynamic trapping, [Phys. Rev. Lett. \*\*106\*\*, 198104 \(2011\)](#).
- [7] N. Khurana and N. T. Ouellette, Interactions between active particles and dynamical structures in chaotic flow, [Phys. Fluids \*\*24\*\*, 091902 \(2012\)](#).
- [8] R. Rusconi, J. S. Guasto, and R. Stocker, Bacterial transport suppressed by fluid shear, [Nat. Phys. \*\*10\*\*, 212 \(2014\)](#).
- [9] W. M. Durham, E. Climent, M. Barry, F. De Lillo, G. Boffetta, M. Cencini, and R. Stocker, Turbulence drives microscale patches of motile phytoplankton, [Nat. Commun. \*\*4\*\*, 2148 \(2013\)](#).
- [10] M. Borgnino, K. Gustavsson, F. De Lillo, G. Boffetta, M. Cencini, and B. Mehlig, Alignment of nonspherical active particles in chaotic flows, [Phys. Rev. Lett. \*\*123\*\*, 138003 \(2019\)](#).
- [11] N. Pujara, M. A. R. Koehl, and E. A. Variano, Rotations and accumulation of ellipsoidal microswimmers in isotropic turbulence, [J. Fluid Mech. \*\*838\*\*, 356 \(2018\)](#).
- [12] B. Qin and P. E. Arratia, Confinement, chaotic transport, and trapping of active swimmers in time-periodic flows, [Sci. Adv. \*\*8\*\*, eadd6196 \(2022\)](#).
- [13] X. Si and L. Fang, Preferential alignment and heterogeneous distribution of active nonspherical swimmers near lagrangian coherent structures, [Phys. Fluids \*\*33\*\*, 073303 \(2021\)](#).
- [14] S. A. Berman, J. Buggeln, D. A. Brantley, K. A. Mitchell, and T. H. Solomon, Transport barriers to self-propelled particles in fluid flows, [Phys. Rev. Fluids \*\*6\*\*, L012501 \(2021\)](#).
- [15] X. Si and L. Fang, Preferential transport of swimmers in heterogeneous two-dimensional tur-

- bulent flow, [Phys. Rev. Fluids](#) **7**, 094501 (2022).
- [16] M. E. Huntley and M. Zhou, Influence of animals on turbulence in the sea, [Mar. Ecol. Prog. Ser.](#) **273**, 65 (2004).
- [17] E. Kunze, J. F. Dower, I. Beveridge, R. Dewey, and K. P. Bartlett, Observations of biologically generated turbulence in a coastal inlet, [Science](#) **313**, 1768 (2006).
- [18] K. Katija and J. O. Dabiri, A viscosity-enhanced mechanism for biogenic ocean mixing, [Nature](#) **460**, 624 (2009).
- [19] A. W. Visser, Biomixing of the oceans?, [Science](#) **316**, 838 (2007).
- [20] I. A. Houghton, J. R. Koseff, S. G. Monismith, and J. O. Dabiri, Vertically migrating swimmers generate aggregation-scale eddies in a stratified column, [Nature](#) **556**, 497 (2018).
- [21] R. Ouillon, I. A. Houghton, J. O. Dabiri, and E. Meiburg, Active swimmers interacting with stratified fluids during collective vertical migration, [J. Fluid Mech.](#) **902**, A23 (2020).
- [22] X. Si and L. Fang, Biologically generated turbulent energy flux in shear flow depends on tensor geometry, [PNAS Nexus](#) **3**, pgae056 (2024).
- [23] X. Si and L. Fang, Interaction between swarming active matter and flow: the impact on lagrangian coherent structures, [Phys. Rev. Fluids](#) **9**, 033101 (2024).
- [24] G. Haller, Lagrangian coherent structures, [Annu. Rev. Fluid Mech.](#) **47**, 137 (2015).
- [25] G. Haller and G. Yuan, Lagrangian coherent structures and mixing in two-dimensional turbulence, [Physica D](#) **147**, 352 (2000).
- [26] S. C. Shadden, F. Lekien, and J. E. Marsden, Definition and properties of lagrangian coherent structures from finite-time lyapunov exponents in two-dimensional aperiodic flows, [Physica D](#) **212**, 271 (2005).
- [27] N. T. Ouellette and J. P. Gollub, Curvature fields, topology, and the dynamics of spatiotemporal chaos, [Phys. Rev. Lett.](#) **99**, 194502 (2007).
- [28] G. Boffetta and R. E. Ecke, Two-dimensional turbulence, [Annu. Rev. Fluid Mech.](#) **44**, 427 (2012).
- [29] D. H. Kelley and N. T. Ouellette, Onset of three-dimensionality in electromagnetically driven thin-layer flows, [Phys. Fluids](#) **23**, 045103 (2011).
- [30] L. Fang and N. T. Ouellette, Influence of lateral boundaries on transport in quasi-two-dimensional flow, [Chaos](#) **28**, 023113 (2018).
- [31] N. T. Ouellette, P. J. J. O'Malley, and J. P. Gollub, Transport of finite-sized particles in

chaotic flow, [Phys. Rev. Lett.](#) **101**, 174504 (2008).

- [32] N. T. Ouellette, H. Xu, and E. Bodenschatz, A quantitative study of three-dimensional lagrangian particle tracking algorithms, [Exp. Fluids](#) **40**, 301 (2006).